

REPORT DOCUMENTATION PAGE				Form Approved OMB No. 0704-0188	
<small>The public reporting burden for this collection of information is estimated to average 1 hour per response, including the time for reviewing instructions, searching existing data sources, gathering and maintaining the data needed, and completing and reviewing the collection of information. Send comments regarding this burden estimate or any other aspect of this collection of information, including suggestions for reducing the burden, to the Department of Defense, Executive Services and Communications Directorate (0704-0188). Respondents should be aware that notwithstanding any other provision of law, no person shall be subject to any penalty for failing to comply with a collection of information if it does not display a currently valid OMB control number.</small> <b>PLEASE DO NOT RETURN YOUR FORM TO THE ABOVE ORGANIZATION.</b>					
1. REPORT DATE (DD-MM-YYYY)		2. REPORT TYPE FINAL REPORT		3. DATES COVERED (From - To) 15 MAY 2001 - 31 JUL 2006	
4. TITLE AND SUBTITLE EXPLOITING ADAPTIVE OPTICS WITH DEFORMABLE SECONDARY MIRRORS				5a. CONTRACT NUMBER	
				5b. GRANT NUMBER F49620-01-1-0383	
				5c. PROGRAM ELEMENT NUMBER 61102F	
				5d. PROJECT NUMBER 2301/GX	
6. AUTHOR(S) DR HART				5e. TASK NUMBER	
				5f. WORK UNIT NUMBER	
7. PERFORMING ORGANIZATION NAME(S) AND ADDRESS(ES) UNIVERSITY OF ARIZONA PO BOX 3308 TUCSON Z 85722-3308				8. PERFORMING ORGANIZATION REPORT NUMBER	
9. SPONSORING/MONITORING AGENCY NAME(S) AND ADDRESS(ES) AF OFFICE OF SCIENTIFIC RESEARCH 875 NORTH RANDOLPH STREET ROOM 3112 ARLINGTON VA 22203 DR ANNE MATSUURA/NE				10. SPONSOR/MONITOR'S ACRONYM(S)	
				11. SPONSOR/MONITOR'S REPORT NUMBER(S)	
12. DISTRIBUTION/AVAILABILITY STATEMENT DISTRIBUTION STATEMENT A: UNLIMITED				AFRL-SR-AR-TR-07-0132	
13. SUPPLEMENTARY NOTES					
14. ABSTRACT The major thrust of our research program has been to start the development of multiple laser beacon systems for wavefront sensing, and to tie this new technology to the unique development of deformable secondary mirrors pioneered at the University of Arizona's Center for Astronomical Adaptive Optics (CAAO). The technology development funded by this award has resulted in the first practical solution for a multi-beacon laser system, enabling progress in tomographic wavefront sensing and altitude conjugated adaptive correction, and is a critical step forward for adaptive optics for future large telescopes proposed for very high resolution space situational awareness. This has been demonstrated by the first high resolution images of geostationary satellites, captured at the 6.5 m MMT telescope, using the deformable secondary adaptive optics system.					
15. SUBJECT TERMS					
16. SECURITY CLASSIFICATION OF:			17. LIMITATION OF ABSTRACT	18. NUMBER OF PAGES	19a. NAME OF RESPONSIBLE PERSON
a. REPORT	b. ABSTRACT	c. THIS PAGE			19b. TELEPHONE NUMBER (Include area code)



\$B

NE



## Final Technical Report

AFOSR award

F49620-01-1-0383

### Exploiting Adaptive Optics with Deformable Secondary Mirrors

The University of Arizona

Tucson, AZ 85721

March 8, 2007

#### **DISTRIBUTION STATEMENT A**

Approved for Public Release

Distribution Unlimited

# 20070426203

## Contents

1. Program Overview	3
2. Motivation	4
3. System Description	4
3.1. Laser projector system	4
3.2. Dynamic refocus system	5
3.3. Wavefront sensors and tomographic computation hardware	5
4. Results	6
4.1. Ground-layer sensing	7
4.2. Tomographic reconstruction along a single line of sight	9
4.3. Synthetic point-spread functions	12
4.4. GEO satellite observations	14
5. Conclusions	15
6. References	16

## 1. Program Overview

The major thrust of our research program has been to start the development of multiple laser beacon systems for wavefront sensing, and to tie this new technology to the unique development of deformable secondary mirrors pioneered at the University of Arizona's Center for Astronomical Adaptive Optics (CAAO). The technology development funded by this award has resulted in the first practical solution for a multi-beacon laser system, enabling progress in tomographic wavefront sensing and altitude conjugated adaptive correction, and is a critical step forward for adaptive optics for future large telescopes proposed for very high resolution space situational awareness. This has been demonstrated by the first high resolution images of geostationary satellites, captured at the 6.5 m MMT telescope, using the deformable secondary adaptive optics system.

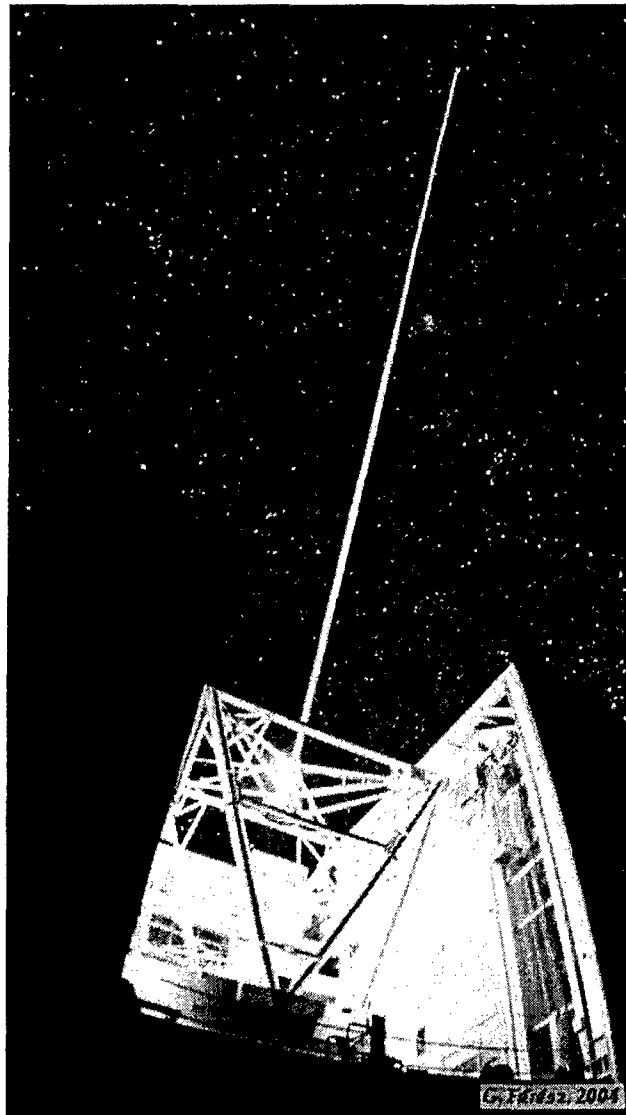


Figure 1. The five laser beams, generated from two 15 W doubled-YAG lasers, projected from behind the secondary mirror of the 6.5 m MMT telescope.

The system now being tested at the MMT has been designed to be the simplest possible to make the first implementation of the tomography image compensation method. We report results from telescope runs at the MMT, which demonstrate for the first time not only tomographic sensing of the atmospheric wavefront, but a new technique called ground-layer sensing in which low-level atmospheric turbulence is isolated. Correction of just this contribution to the atmospheric aberration would result in partially corrected images, but over a field of view much larger than that delivered by conventional adaptive optics.

## 2. Motivation

Key advances in adaptive optics (AO) will be enabled through the deployment of multiple laser guide stars (LGS). Constellations of beacons may be analyzed to yield a three-dimensional solution to the atmospherically induced wavefront aberration through tomography. Wider compensated fields of view than are now seen with conventional AO systems, even those equipped with single laser beacons, will be achieved with less field dependence of the delivered point-spread function. Multi-conjugate AO (MCAO) using tomographic wavefront sensing is expected to yield correction to the diffraction limit in the near infrared over fields of 1–2 arc minute diameter. Compensation of turbulence close to the ground is anticipated to give substantial improvement over natural seeing for even larger fields up to 10 arc minutes.

The promise of these new techniques, which remain almost entirely unexplored at any telescope, is even greater for the next generation of extremely large telescopes (ELTs) (Johns et al. 2004). Indeed, a key motivation for our work at the MMT telescope described here is to understand how to design, build, and operate AO systems for these giant telescopes, where multi-LGS tomographic wavefront sensing will be essential. Because laser beacons are at finite height in the atmosphere, rays of light from LGS sample the atmosphere differently from rays of starlight. The resulting difference between wavefronts measured from a natural star and those from an LGS pointed in the same direction is called focal anisoplanatism. For current telescopes, the error is not so large as to prevent high Strehl imaging in the near infrared with a single LGS, but the error grows with aperture, and for ELTs the error would be prohibitive. It can be overcome however by combining signals from multiple LGS which collectively fill the volume of atmosphere perturbing the starlight.

Current AO systems that rely entirely on the object of interest itself for wavefront information suffer from a severe restriction on the brightness of the objects that can be imaged at high resolution. In contrast, the gains from multi-LGS systems will be realizable with almost any object, enormously expanding the reach of government and astronomical telescopes.

## 3. System Description

### 3.1. Laser projector system

The system employs two 15 W lasers from Lightwave Electronics, operating at 532 nm (frequency doubled YAG) at 5 kHz rep rate. The two linearly polarized beams are combined with a polarizing beam splitter to

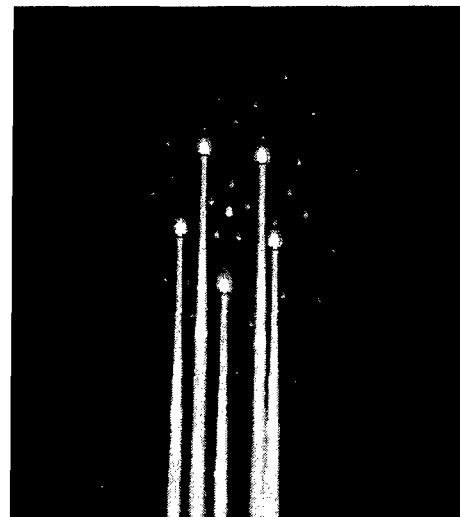


Figure 2. The laser beams projected on a 1 arc minute radius, using a custom hologram. The beams are here seen on the bottom of cloud. Approximately 80% of the power is in the five beams.

produce a single, diffraction-limited beam of 30 W. In operation, synchronized pulses of light from the lasers are split by a computer generated hologram in the projection telescope to create the 5 beacons on a 2 arc minute diameter ring on the sky. The lasers and combining optics are attached directly to the 6.5 m telescope tube, with the power supplies and chiller in the adjacent room in the co-rotating MMT building. The laser heads are enclosed in a thermally isolated environment to maintain them at constant temperature. At the top of the telescope tube on one side is a steering mirror close to an image of the exit pupil, used to compensate for slow misalignments in the projected beam direction caused by flexure and temperature changes. The hologram is also at this pupil. The beams are launched together (Figure 2) through one 50 cm diameter telephoto-type objective mounted centrally on the 6.5 m telescope axis, directly above the adaptive secondary.

### 3.2. *Dynamic refocus system*

This system is to increase the depth of field of all 5 beacons, by refocusing the telescope dynamically in order to follow the conjugate of each pulse of laser light as it rises at the speed of light. The five synchronized beacons are imaged through fast optics to form a single pupil on an oscillating retro-reflecting mirror (Figure 3). The mechanical oscillator that moves the mirror has a Q of  $\sim 5000$ , and functions as the system's master clock, triggering the lasers to fire and the WFS camera to open its shutter at preset phase lags. These are chosen so that during the 60 microsecond interval that light is returned from 20 to 29 km, the mirror motion holds the image of the beacons in sharp focus.

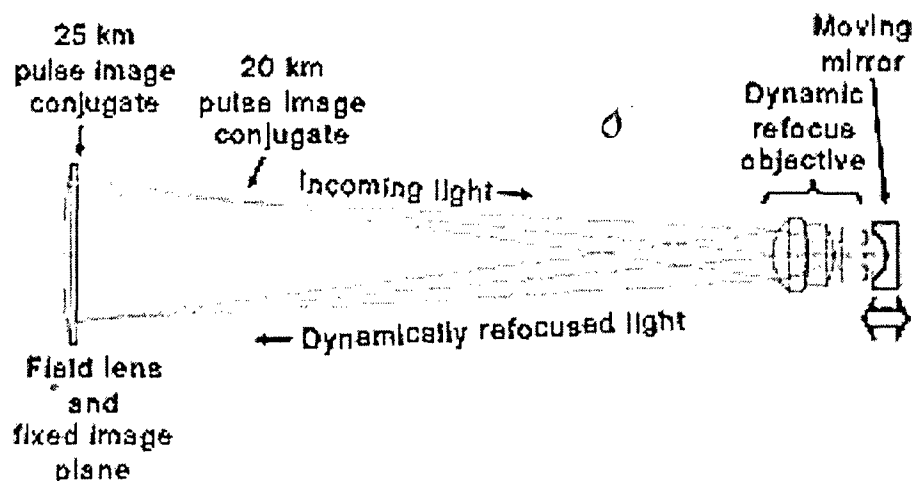


Figure 3. Design for the dynamic refocus optics, as deployed on the MMT.

### 3.3. *Wavefront sensors and tomographic computation hardware*

For the LGS wavefront sensor, the five separate laser wavefronts are analyzed by five Shack-Hartmann spot patterns imaged on a single CCD array. The detector, from MIT Lincoln Lab, is a  $128 \times 128$  CCID18 with  $21 \mu\text{m}$  pixels and electronic shuttering. This device is unique in providing the essential feature of fast gating, so that only light returning from the 20-29 km range of altitudes is accepted on the wavefront sensor. The CCD is driven by a controller from SciMeasure, with 16 parallel outputs, each read at 1 MHz pixel rate, for a maximum frame rate of 915/sec. The hexapolar subaperture geometry is created with a faceted prism array cut from

acrylic and held in index-matching oil tuned to provide the desired angular deflection for each facet. A prism array implementing 60 subapertures has been made and is routinely used on the sky (Figure 4).

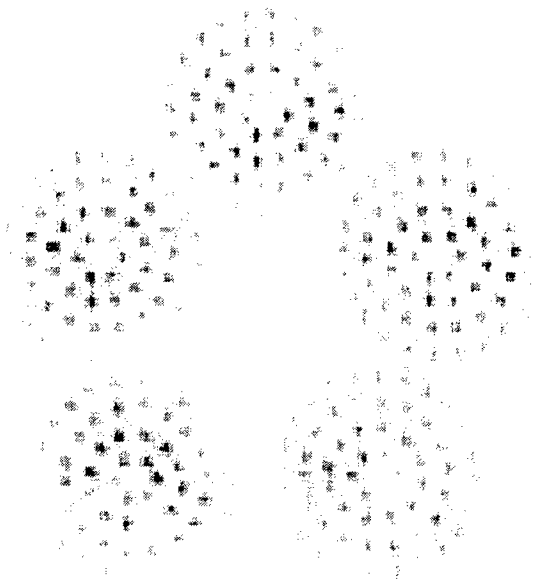


Figure 4. Example of data from the RLGS WFS showing the 60 subaperture Shack-Hartmann patterns made by the five laser beacons.

For ground-truth natural star wavefront measurements, a beamsplitter mirror before the dynamic refocus mechanism directs starlight to a separate Shack-Hartmann WFS. This is identical to the unit used in the MMT NGS system, with  $12 \times 12$  subapertures and 550 Hz frame rate.

Because the beacons are all at a common range of altitude, it is impossible to discriminate on the basis of the LGS signals alone between contributions to 2<sup>nd</sup> order modes (focus and astigmatism) arising near the ground and arising in the free atmosphere (Lloyd-Hart & Milton 2003). Since these modes contain the most power after tilt, which is any case not sensed by the lasers, it will be important in a closed-loop MCAO system to solve for these modes tomographically. This can be done by sensing the differential motion of three stars in the field, which is sensitive to wavefront curvature at high altitude (Rigaut, Ellerbroek, & Flicker 2000). In addition to the NGS and LGS wavefront sensor cameras therefore, a fast-framing camera with 3 arc minute field is used to sense global tilt on several stars at once.

Data from all the sensors are recorded simultaneously in PC computer systems, with synchronization provided by frame counters embedded in the first pixel of each data frame. Real-time processing of the wavefront sensor data for closed loop tomographic operation requires a computer capable of sustained calculation at 20 Gflops. The custom-built machine to do this is based on the Analog Devices TigerSharc DSP.

#### 4. Results

In this section we summarize a variety of results that have been obtained with the system. The unique capabilities of the laser-guided system are described, as tested in telescope runs from mid-2004 through mid-2006. We cover the new techniques of ground-layer correction for wide-

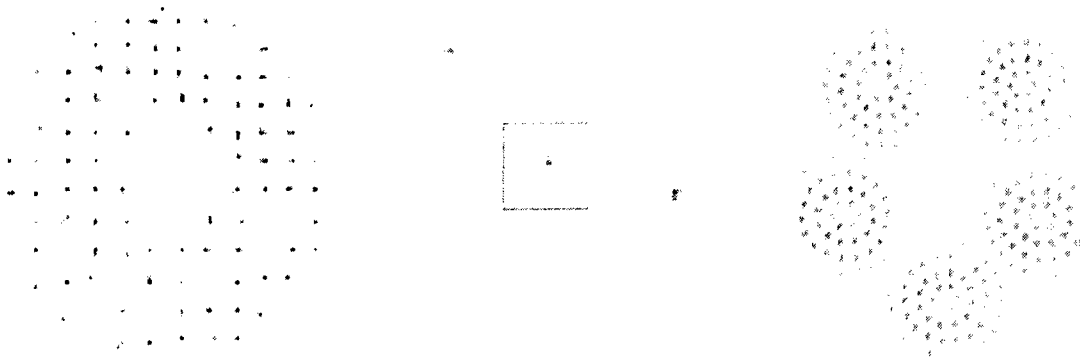


Figure 5. Sample data from the three real-time cameras and the corresponding reconstructed wavefronts. On the top row, from left to right, continuous and simultaneous sequences of frames from the NGS Shack-Hartmann sensor, the wide field asterism camera, and the LGS Shack-Hartmann sensor. (The star images in the asterism have been magnified  $\times 4$  compared to their spacing.) The boxed star in the asterism is the same as used on the NGS sensor; the light is split between the two. The lower panels show the reconstructed NGS wavefront (left), the individual LGS wavefronts (right) and the NGS wavefront as estimated by tomography (center).

field high-resolution imaging, tomography for all-sky imaging at the diffraction limit, and recent results in high-resolution imaging of geostationary satellites.

#### 4.1. *Ground-layer sensing*

The ground layer contribution to stellar wavefront aberration is computed as the average of the wavefronts reconstructed from the individual LGS beacons. Atmospheric turbulence close to the ground is common to the star and each LGS beacon, while higher altitude aberration, different for each beacon, will be reduced in the average. Since all field points share this common ground layer turbulence, the use of GLAO promises a reduction of wavefront aberration over a wide field. The technique is likely to be valuable because it is found empirically that up to two thirds of atmospheric turbulence is typically located near the ground (Verin et al. 2000).

Wavefront recoveries using this approach, under seeing conditions of  $\sim 1.1$  arc second, are described in detail in Lloyd-Hart et al. (2005). Since then, we obtained additional data in seeing of  $\sim 0.5$  arc second ( $r_0 = 22$  cm at 500 nm wavelength), at the 15th percentile for the site measured over the past two years. In both cases, the fidelity of the estimation across the field encompassed by the LGS was investigated by offsetting the telescope and the beacons with



respect to the NGS. The ground layer wavefront reconstruction estimated the 25 modes of Zernike orders 2 through 6 from the LGS.

Figure 6 shows the residual stellar wavefront error after GLAO correction as a function of angle from the center of the LGS constellation. Ground layer correction of the data taken in poorer seeing yielded an average 38% improvement in RMS wavefront aberration over the full field enclosed by the beacons, and extended well outside the constellation. For the new data, when the seeing was already excellent, ground layer correction was consistently beneficial across the field, although the fractional improvement within the constellation was actually less at 25%, with correction not extending as far beyond the beacon radius. Across this broad range of conditions, spanning roughly the middle half of the probability density function of seeing at the MMT, the point-spread function (PSF) delivered by a closed-loop system would show morphological variation much less than one would expect from the raw seeing. Furthermore, this result suggests that ground-layer correction with LGS will be a powerful tool for recovering good image quality especially when the native seeing is worse than median.

A key parameter for GLAO is the thickness of the boundary layer, since it determines the corrected field of view. Very little is known about the boundary layer from current site surveys because the GLAO concept is quite recent, and the ground layer thickness has almost no impact on any other observing mode of a telescope. We have estimated the thickness during our observations by a method described in Lloyd-Hart et al. (2005) which examines the anisoplanatic behavior of the stellar wavefront with respect to the individual LGS wavefronts. The RMS difference between the two with angular separation  $\theta$  is expected to grow as  $(\theta/\theta_0)^{5/3}$ . The isoplanatic angle  $\theta_0$  for the ground layer is related to the turbulence-weighted mean height  $h$  of the layer through  $\theta_0 = 0.314 \cos \zeta r_0/h$ . For observations made in September 2004, we find  $h =$

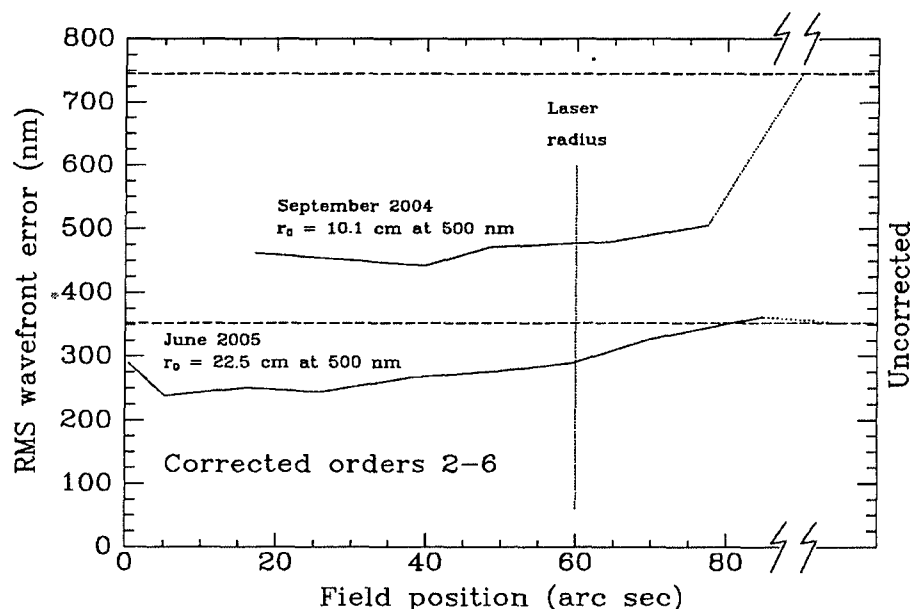


Figure 6. Wavefront correction of starlight on the basis of the average LGS signals. The dashed lines show the uncorrected error while the solid lines show the RMS residual wavefront phase after ground layer correction as a function of angular distance between the star and the geometric center of the LGS constellation. Tilt (global image motion) is excluded since it is not sensed by the lasers.

380 m. For data recorded in June 2005, despite the lower absolute strength of the ground layer, its mean height was greater, with  $h = 530$  m.

#### 4.2. Tomographic reconstruction along a single line of sight

The tomographic solution of the beacon wavefronts in principle yields a three-dimensional view of the aberration. In the simplest application, the instantaneous wavefront from an astronomical object is estimated by integration through the volume along the line of sight to the object, and the compensating phase is applied to a single deformable mirror. The technique, called laser tomography AO (LTAO), delivers a diffraction-limited field of view limited by the normal isoplanatic angle. Each of the steps of this process, illustrated in Figure 7, is linear. In practice therefore, all the steps may be multiplied to give a single linear function. In this way, LTAO can be implemented in a conventional way through a matrix multiplication of the combined vector of slopes from all the beacons to yield a command update to the DM. For clarity in our analysis, we have chosen first to reconstruct separately the wavefronts from each of the LGS and then to apply a tomographic reconstructor matrix to estimate the wavefront of the probe star.

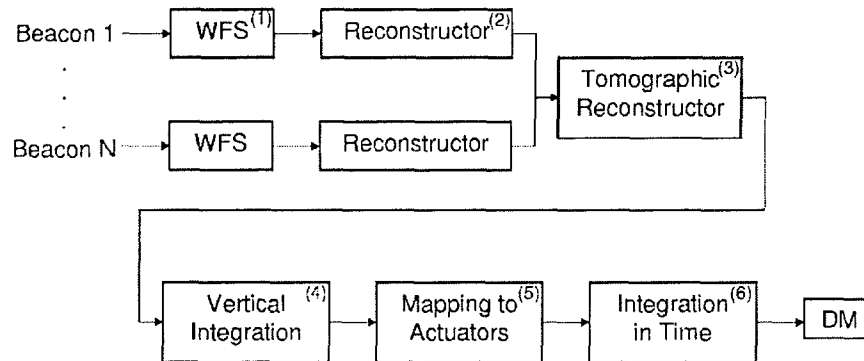


Figure 7. The processing sequence for laser tomography AO. Light from each beacon is recorded by a wavefront sensor (1), and the individual beacon wavefronts are reconstructed (2). The three-dimensional structure of the aberration is recovered by tomography (3). A spatial integration along the line of sight estimates the stellar aberration (4), which is mapped onto the DM actuators (5) and (in a closed-loop AO system) integrated in time to give the required actuator commands (6). In practice, steps (2) through (5) can be implemented as a single matrix-vector multiplication.

Data from the three real-time cameras have been analyzed in this way. Spot positions in the Shack-Hartmann patterns recorded on the LGS WFS were extracted frame by frame to a precision of 0.03 pixels (0.026 arcsec) by finding the local peaks in the correlation of the data with a gaussian of width 1.8 pixels. For each 60 s data set, the mean position of each spot was subtracted from its instantaneous position, thereby removing the effects of telescope aberration and long-term collimation drift. Wavefronts from each LGS were then reconstructed from the residual spot positions by fitting the first 44 Zernike modes (orders 1 through 8) using a synthetic reconstructor matrix derived from a model of the prism array in the WFS optics.

In a closed-loop system, the reconstructed LGS tilt modes would be used to control beam jitter by driving a fast steering mirror in the laser beam projector optics, but for this open-loop analysis they are discarded. Instead, the higher order LGS measurements are supplemented by the image

motion from three stars in the wide field asterism camera, shown in Figure 8. The stars allow determination of the tilt terms in the central probe star's wavefront, and a three-dimensional solution to the second-order terms focus and astigmatism (Lloyd-Hart & Milton 2003). Separately, the wavefronts from the probe star were reconstructed to the same order from the NGS sensor measurements. For comparison, a ground layer estimate of the probe star's wavefront was also reconstructed from these data.

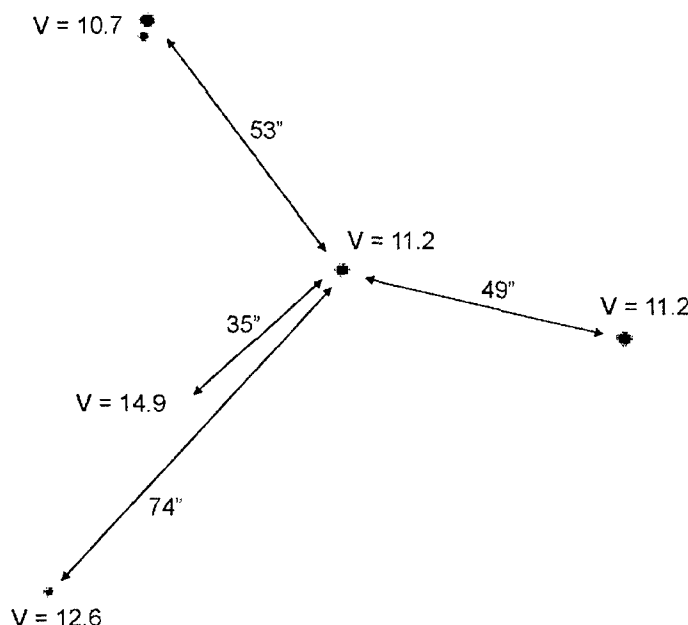


Figure 8. Sample frame from the asterism camera. Light from the central star was also fed to the NGS WFS. Image motion of the three brightest stars surrounding this one were used to estimate global tilt and second order modes in the tomographic reconstruction. The positions of the beacons are illustrated by the green stars. To account for field rotation, the LGS pattern was rotated in the beam projector optics, maintaining a fixed orientation with respect to the asterism as the MMT tracked.

Our tomographic reconstruction assumes a linear relation between the wavefront of the probe star and those of the LGS, represented by the equation

$$\hat{\mathbf{a}} = \mathbf{T} \mathbf{b}$$

where  $\hat{\mathbf{a}}$  is the vector of Zernike polynomial coefficients characterizing the estimate of the probe star wavefront,  $\mathbf{b}$  is a vector containing the Zernike coefficients of all the reconstructed LGS wavefronts and the tilt measurements from the three field stars, and  $\mathbf{T}$  is the tomographic reconstructor matrix relating the two. We wish to find a tomograph  $\mathbf{T}$  that minimizes  $\langle |\mathbf{a} - \hat{\mathbf{a}}|^2 \rangle$ , the squared norm of the difference between the measured probe star wavefront coefficients  $\mathbf{a}$  and their estimates, averaged over time. The coefficients are scaled so that this also minimizes the RMS residual phase in the reconstructed wavefront.

To investigate the limit of tomographic performance permitted by the data in this least squares sense, we have derived  $\mathbf{T}$  by a direct inversion of the data, using singular value decomposition

(SVD). This approach does not rely on any *a priori* model of the atmospheric  $C_n^2$  profile or knowledge of the noise characteristics. A matrix  $\mathbf{B}$  is constructed from 3057 data vectors  $b$ , and inverted with SVD to give  $\mathbf{B}^\dagger$ . A similar matrix  $\mathbf{A}$  is constructed from the corresponding  $\mathbf{a}$  vectors. The tomograph is then given by

$$\mathbf{T} = \mathbf{A} \mathbf{B}^\dagger.$$

Applying  $\mathbf{T}$  to vectors  $b$  drawn from the same data set used to compute it yields the best fit solution and characterizes the noise floor in the data.

The noise sources fall into two broad categories. The first comprises instrumental effects such as read noise and charge diffusion in the WFS, and photon noise from the lasers. These can be reduced by better (and generally more expensive) hardware. The second arises because of atmospheric effects: broadening of the LGS images by turbulence in the uplink, speckle structure in the NGS Shack-Hartmann sensor spots, and aliasing of high altitude aberrations that are not well sensed by the chosen LGS constellation. These are more difficult to overcome. A full evaluation of these in the context of the MMT experiments is now underway.

We find, as expected, that our tomographic approach yields a substantially better estimate of the probe star's wavefront than the corresponding ground layer recovery. To illustrate, Figure 9 shows the evolution of the focus term in the probe star's wavefront over a 10 s period and its GLAO and LTAO estimates. Figure 10a shows the RMS wavefront error averaged over the full 60 s of each of 9 data sets, recorded over a period of 2 hours. The values reflect the contributions from the modes through order 8 that were reconstructed, with the exception of tip and tilt. These two modes contain the majority of the wavefront error, but are not sensed by the lasers and therefore give a somewhat misleading sense of the overall degree of correction.

Values of  $r_0$  for each data set are shown in Figure 10b at a wavelength of 500 nm and corrected to zenith. We start by computing values for the mean square aberration in the modes of each Zernike radial order separately. Applying the formalism developed by Chassat (1992) then yields estimates of both  $r_0$  and the outer scale of turbulence  $L_0$ . Our estimates of  $L_0$  range from 12 m to 25 m over the 2 hour period during which the data were recorded, in line with other observations at good sites (Fusco et al. 2004). (We note in passing that the variable directly estimated by Chassat's method is  $D/L_0$ , where  $D$  is the telescope diameter. The truncated forms

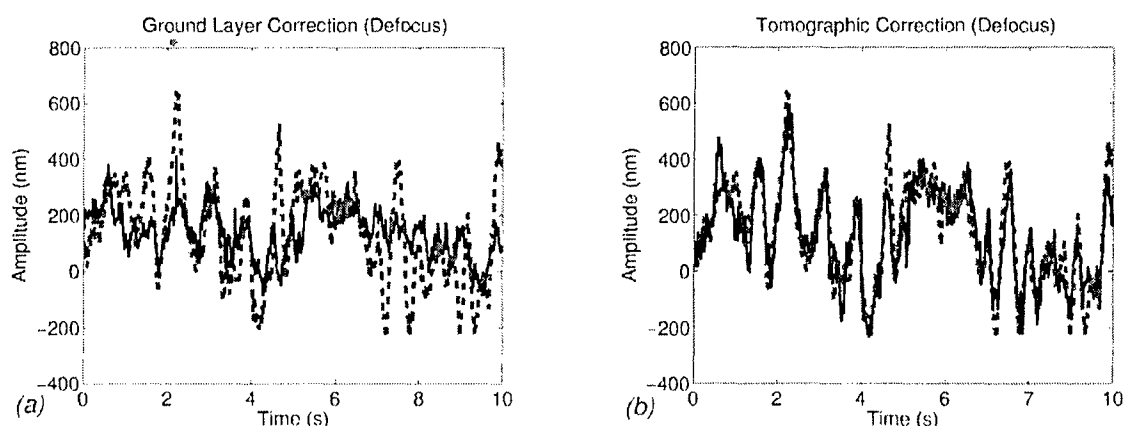


Figure 9. Evolution of focus in the probe star's wavefront, shown in blue on the two plots, with the ground layer estimate (a) and tomographic estimate (b) plotted in black.

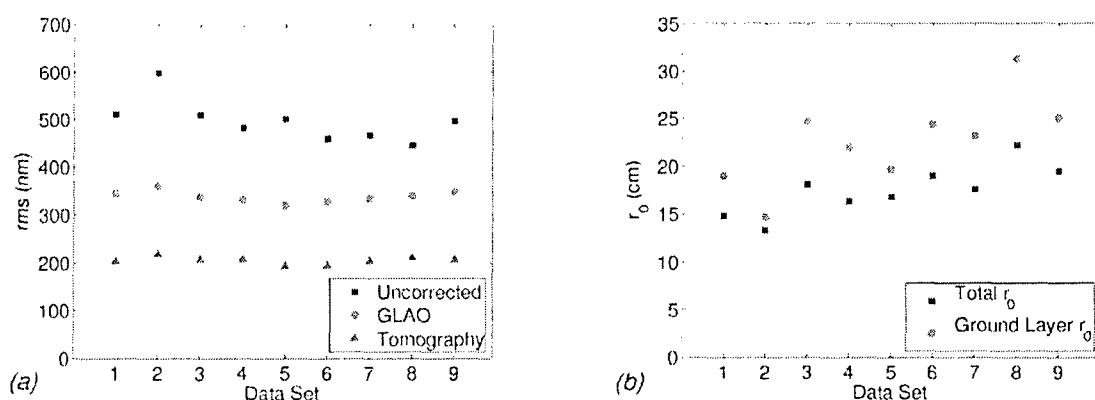


Figure 10. For each of 9 data sets, each 60 s long, (a) shows the RMS wavefront error summed over orders 2–8 for the probe star wavefront without correction (blue squares), and with GLAO (red circles) and LTAO (green triangles) correction. Values of  $r_0$ , shown in (b) for a wavelength of 500 nm at zenith, have been computed for the total seeing (blue squares) and the ground layer contribution (red circles) only. The data sets were recorded over a 2 hour period and are here numbered chronologically.

of the infinite sums given by Chassat and Fusco, appropriate for the small apertures used in those studies, must be extended in our case where  $D/L_0 > 0.25$ .)

Also shown in Figure 10b are values for the ground layer turbulence, computed in the same manner from the strength of the Zernike modes of the ground layer estimate from the LGS. We find the average distribution of turbulence for these data puts 70% of the power in the boundary layer with the remainder at higher altitude. This represents an upper limit, since high altitude aberration on large spatial scales will remain partially correlated in the LGS signals and be indistinguishable from true ground layer aberration.

The plots of Figure 10 show a consistent improvement with both types of wavefront compensation. Of particular note is data set 2, which stands out from its neighbors as having distinctly worse seeing. Yet after ground layer correction, the residual aberration is reduced almost to the same level in all three cases, indicating that the momentary worsening was attributable to a low lying phenomenon.

#### 4.3. Synthetic point-spread functions

From the residual wavefront errors after either ground layer or tomographic estimation at each time step, a synthetic corrected PSF can be calculated. Figure 11 shows examples computed for a source on axis at 2.2  $\mu\text{m}$  wavelength from a 60 s continuous data sequence recorded in seeing conditions of  $r_0 = 14.7$  cm at 500 nm wavelength. The reconstruction estimated the first 44 modes of the probe star's wavefront, now including tip-tilt. To generate realistic instantaneous PSFs, the wavefronts were augmented with temporally correlated Zernike modes from orders 9 through 30 drawn from an uncompensated Kolmogorov distribution. The integrated PSFs in Figure 11 include uncompensated Zernike modes from orders 9 through 100.

Table 1 below shows the corresponding widths and relative peak intensities for the time averaged PSFs, and for PSFs computed similarly at 1.25  $\mu\text{m}$  and 1.65  $\mu\text{m}$ . Ground layer correction is of particular value in the two longer wavebands, where the image width is reduced by a factor of

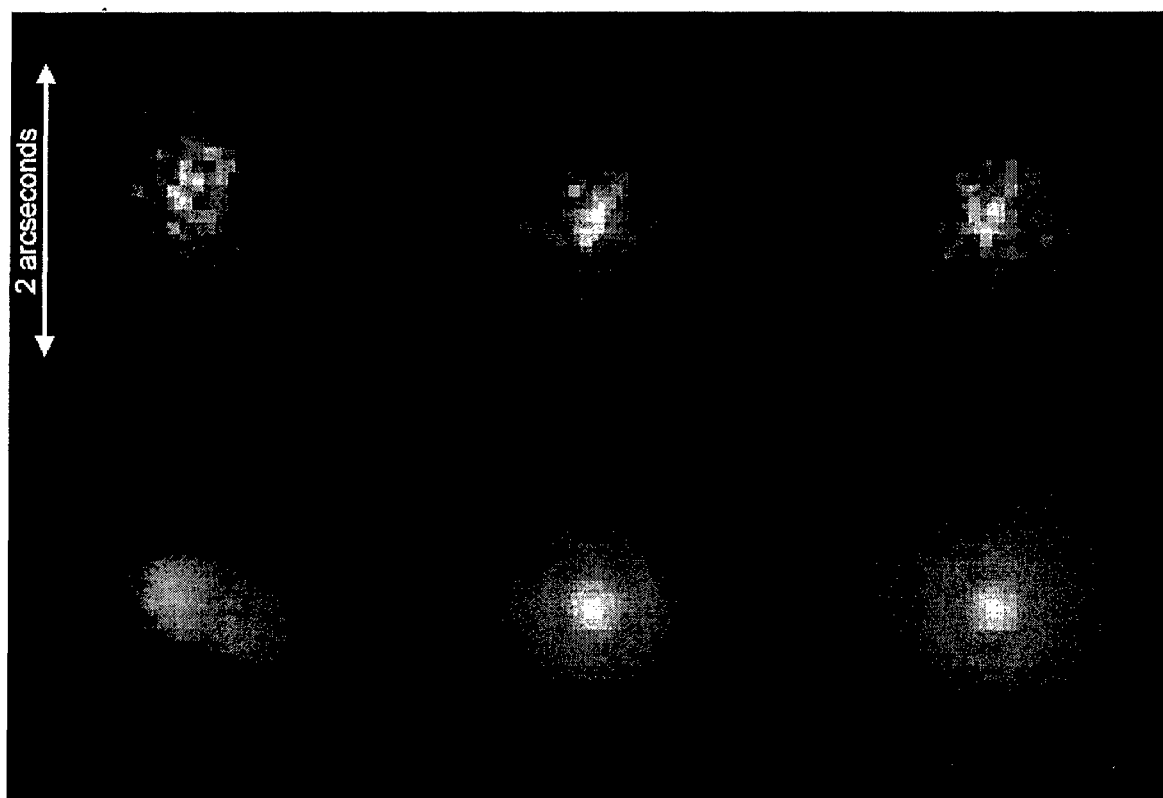


Figure 11. Synthetic point-spread functions computed at  $2.2\ \mu\text{m}$  wavelength from wavefronts before and after correction. The top row shows examples of instantaneous PSFs; the lower panels show PSFs averaged over the full 60 s sequence. (Left) PSFs with no correction; (center) with GLAO correction; (right) with LTAO correction.

$\sim 4$ , and there is a substantial increase in peak intensity. Given that the seeing at the time the data were taken was at about the 50th percentile for the telescope, one can expect closed-loop GLAO performance at  $\sim 0.2$  arc second or better at wavelengths beyond  $1.5\ \mu\text{m}$  for the majority of the time.

Metric	Waveband ( $\mu\text{m}$ )	Uncorrected	GLAO	LTAO	Diffraction limit
FWHM (arc sec)	1.25	0.77	0.38	0.110	0.040
	1.65	0.68	0.17	0.086	0.052
	2.20	0.55	0.12	0.089	0.070
Relative peak intensity	1.25	1.0	2.0	3.9	498
	1.65	1.0	3.7	9.4	239
	2.20	1.0	7.0	15.0	92

Table 1. Image quality metrics at near infrared wavelengths.

With tomographic correction, imaging at  $2.2\ \mu\text{m}$  is corrected almost to the diffraction limit, with a 14-fold increase in peak intensity to a Strehl ratio of 16%. The relatively low order reconstruction is insufficient to achieve the diffraction limit at the shorter wavelengths, but the improvement in resolution and peak brightness are both substantial.

#### 4.4. GEO satellite observations

To demonstrate the capabilities of the AO system we have obtained a data set on two bright GEO satellites. The two satellites we chose to observe were the Canadian communications satellites Anik F-2 launched 17 Jul 2004 and the MSAT M-1 launched 20 Apr 1996. Particularly the Anik F-2 represents an interesting test target as it has solar panels extending almost 50 m in one dimension ( $48\times 8\ \text{m}$  size). By comparison MSAT M-1 is  $21\times 19\ \text{m}$ . A series of data at low airmass consisting of several exposure times in the spectral H band at  $1.6\ \mu\text{m}$  was obtained for each satellite along with corresponding point source star data. Both objects were clearly resolved, as seen in Figure 12 which shows a ground-truth diagram of Anik F-2 and an AO corrected image from the telescope. We note that the diffraction limit for the MMT in the infrared corresponds to about 10 m at GEO – so only relatively large satellites are observable with this approach. Nonetheless we believe these may be the first direct ground-based optical images of GEO satellites.

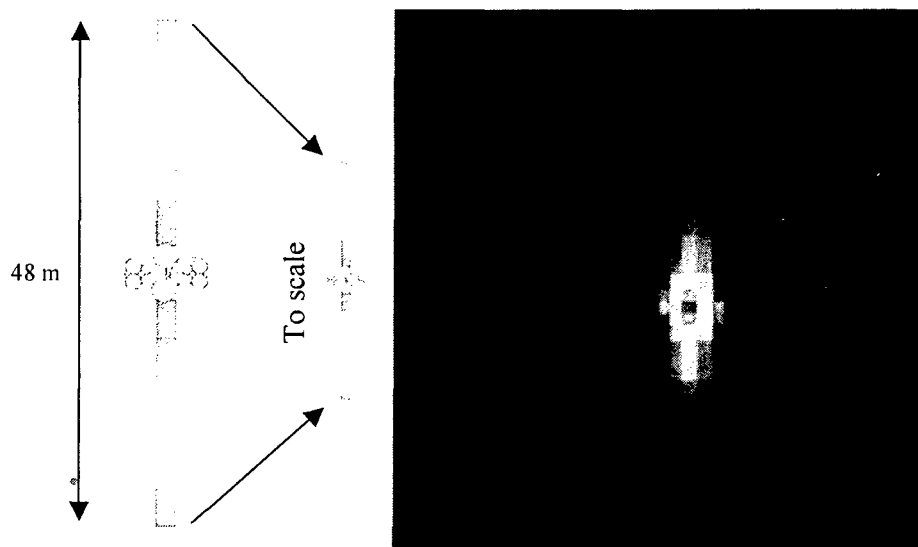


Figure 12. (Left) A rendition of the true appearance of the GEO satellite Anik F-2. (Right) The restored image from the 6.5 m MMT with adaptive optics. One pixel corresponds to 0.017 arc second, or 3.2 m at the range of the satellite.

The recorded images were narrow-band (only 1% bandwidth) and 30 s integration: equivalent to a 3 s exposure in the full H band. Anik F2 was  $H = 9.3$  magnitudes at the time of the observations, making it among the brightest objects in the GEO belt, a reason for using it as an optimum test target. The noise in the halo of light at 0.5 arc second away in the AO-corrected image is approximately  $500\times$  fainter than the satellite, or approximately  $H = 16$ . The noise is random, obeying photon statistics. Longer integrations can therefore easily achieve fainter detection limits. Thus we believe microsatellites could be readily detected with this system.

To reach the limits of microsatellite detection, sophisticated post-processing methods that are applicable to AO-corrected image data are required. We have worked in partnership with the

University of Hawai'i to develop such algorithms (Jefferies et al. 2005, Hope et al. 2005) which can provide further improvements in the image resolution. We used these methods to post-process our satellite data. First, multiple images were registered and co-added. An estimate of the noise was then derived and the images Wiener filtered. The Wiener filtered estimate of the target object was then used as the initial estimate for the object in a multi-frame blind deconvolution processing (MFBD) of the data using the algorithm described in Jefferies et al. (2005). The resulting estimates of the point spread functions from the MFBD analysis were then used in the deconvolution algorithm described in Hope et al. (2005) to provide the restoration shown in Figure 12. Simple modeling of the target objects shows that the restorations are close to diffraction limited. Moreover, the level of restoration noise is very low, an important requirement for detecting low intensity objects in the background.

Since one of our objectives is to detect small objects near large ones we have examined our data to determine how well a small object might be detectable in the vicinity of a bright object such as Anik F-2. We artificially placed unresolved objects in the field of the AO corrected image that were fainter by factors of 100 and 300, or 15<sup>th</sup> and 16<sup>th</sup> magnitude respectively. These would be objects with optical cross sections of 0.3–1 m<sup>2</sup>, typical sizes for today's microsatellites. The results are shown in Figure 13. For the latter two test images a radially smoothed component has been removed. The accompanying object is clearly visible in both cases. Based on our results we believe objects up to ten times fainter (19<sup>th</sup> magnitude) and cross sections of a few hundredths of a square meter would be visible with minimal post-processing.

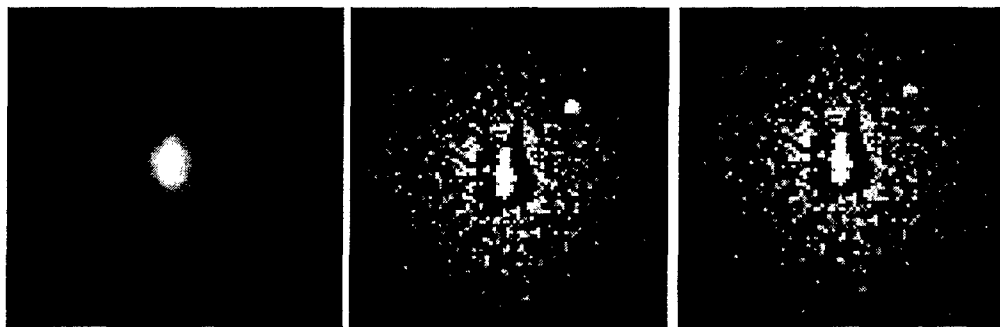


Figure 13. Results of simulations of the ability of the MMT AO system to detect microsatellites placed near to a large satellite such as Anik F-2. The left image is a raw AO output for Anik F-2. For our simulations we removed a radial profile to minimize scattered and uncompensated residual light. The middle image shows our simulation for a 1 m<sup>2</sup> microsatellite and the right image shows the results for a 0.3 m<sup>2</sup> object. In both cases the object is 100 m from the large satellite and would be completely invisible in conventional uncompensated imagery.

## 5. Conclusions

We have taken the first steps in exploring the practical techniques required for tomographic wavefront sensing. With 60 subapertures placed over the MMT's 6.5 m aperture and with the WFS running at 100–200 Hz, both the spatial and temporal scales of the wavefront estimation were well corrected. We can now say with confidence that there are no fundamental obstacles to closed-loop AO systems with multiple LGS driving altitude conjugated correction.

Our own work at the MMT will see the implementation of both GLAO and LTAO with the MMT's adaptive secondary mirror. Both techniques will benefit from extensions of the



reconstructors used for the open loop results to date. The former will likely be improved by a tomographic analysis to identify the ground layer contribution with greater fidelity than the simple average of the LGS wavefronts. This would render more uniform PSFs within the corrected field. Tomographic recovery in general will show improved accuracy and robustness by the incorporation of *a priori* statistical knowledge of the atmospheric aberration and the system noise and optimal linear filtering. The application of these principles, well studied theoretically, to our tomographic data is a high priority for future work.

Early application of the new technology to scientific programs will focus on seeing improvement with GLAO, taking advantage of existing near infrared instrumentation. This choice is motivated by a number of considerations. Not only is GLAO the easiest multi-beacon technique to implement, but the MMT's system is likely to remain unique for several years. The exploitation of routine near infrared seeing of 0.2 arc second or better over a field of several arc minutes is likely to be very productive, both for imaging and high resolution multi-object spectroscopy where the many-fold improvement in encircled energy within 0.2 arc second will be of particular value.

Further exploration of tomography will investigate the components of the algorithm outlined in Figure 6. We will start with the recovery of  $C_n^2$  profiles from two sets of open-loop LGS data, taken close together in time, where the probe star is first on axis and then further out in the field of the LGS constellation. The technique to determine the profiles is very similar to slope detection and ranging (SLODAR, Wilson 2002). The derived profiles will be collapsed into a small number of layers. A tomographic reconstructor matrix will be computed to solve for the instantaneous shapes of DMs taken to be at each of these layers. The tomograph will be applied to the NGS data in the two cases, to explore the fidelity and field dependence of MCAO correction.

Closed-loop LTAO, relying just on the adaptive secondary, will be tested in parallel with GLAO. The hardware required is identical for each, with only the elements of the reconstructor matrix to be changed. This suggests a new avenue for research, in which the corrected field of view and the degree of wavefront compensation are traded against each other according to the demands of the immediate observing program and the prevailing atmospheric conditions. The MMT system will be uniquely placed to explore this parameter space.

Finally, we have shown that large astronomical telescopes equipped with adaptive optics systems can open a unique new dimension in space situational awareness by providing resolved images of deep space satellites. In addition to direct imaging applications, adaptive optics images of large GEO and other deep space satellites might also reveal the presence of very small, so-called microsatellites in the vicinity of larger objects. Such objects can be difficult to detect using other ground-based methods.

## 6. References

- Baranec, C., Lloyd-Hart, M., Milton, M., Stalcup, T., Georges, J., Snyder, M., Putnam, N., and Angel, R., 2004, "Progress towards tomographic wavefront reconstruction using dynamically refocused Rayleigh laser beacons," in *Adaptive Optical Systems Technology*, (Proc. SPIE), 4007, 1129.
- Chassat, F., 1992, *Propagation optique à travers la turbulence atmosphérique. Etude modale de l'anisoplanétisme et application à l'optique adaptative*, PhD thesis, Université Paris-Sud.
- Fusco T., et al., 2004, "NAOS performance characterization and turbulence parameters

estimation using closed-loop data," in *Advancements in Adaptive Optics*, D. Bonaccini, B. L. Ellerbroek, and R. Ragazzoni, eds., Proc. SPIE **5490**, 118.

Hope, D. A., Jefferies, S. M., and Hege, E. K., 2005, "Diffraction-limited image restoration using a new object prior", AMOS Technical Meeting

Jefferies, J. M., Giebink, C. A., and Lloyd-Hart, M., 2005, "Temporal constraints in the blind restoration of high-cadence imagery obtained through atmospheric turbulence," AMOS Technical Meeting.

Johns, M, Angel, J. R. P., Sackett, S., Bernstein, R., Fabricant, D., McCarthy, P., and Phillips, M., 2004, "Status of the Giant Magellan Telescope (GMT) project," in *Ground-Based Telescopes*, J. M. Oschmann, ed., Proc. SPIE **5489**, 441.

Lloyd-Hart, M. and Milton, N. M., 2002, "Design and expected performance of the 6.5 m MMT MCAO system," in *Adaptive Optical Systems Technologies II*, (Proc. SPIE), 4839, 578.

Lloyd-Hart, M. and Milton, N. M., 2003, "Fundamental limits on isoplanatic correction with multiconjugate adaptive optics," JOSA, **20**, 1949.

Lloyd-Hart, M., Baranec, C., Milton, N. M., Stalcup, T., Snyder, M., Putnam, N., and Angel, J. R. P., 2005, "First tests of wavefront sensing with a constellation of laser guide beacons," *Astrophys. J.*, **634**, 679.

Rigaut, F. J., Ellerbroek, B. L., and Flicker, R., 2000, "Principles, limitations and performance of multi-conjugate adaptive optics," in *Adaptive Optical Systems Technology*, (Proc. SPIE), 4007, 1022.

Stalcup, T., Georges, J., Snyder, M., Baranec, C., Putnam, N., Milton, M., Angel, R., and Lloyd-Hart, M., 2004, "Field tests of wavefront sensing with multiple Rayleigh laser guide stars and dynamic refocus," in *Advancements in Adaptive Optics*, (Proc. SPIE), 5490, 1021.

Wilson, R. W., 2002, "SLODAR: measuring optical turbulence altitude with a Shack-Hartmann wavefront sensor," *Mon. Not. R. Astron. Soc.*, **337**, 103.

Verin, J., Agabi, A., Avila, R., Azouit, M., Conan, R., Martin, F., Masciadri, E., Sanchez, L., and Ziad, A., 2000, "Gemini site testing campaign. Cerro Pachon and Cerro Tololo," Gemini RPT-AO-G0094, <http://www.gemini.edu/>.